Perturbation of Electron Velocity Distribution due to Interaction with Chorus Emissions

Miroslav Hanzelka[1,2], Ondřej Santolík[1,2], Yoshiharu Omura[3]

[1]Department of Space Physics, Institute of Atmospheric Physics, Czech Academy of Sciences, Prague, Czech Republic

[2]Faculty of Mathematics and Physics, Charles University, Prague, Czech Republic

[3]Research Institute for Sustainable Humanosphere, Kyoto University, Uji, Japan

Key Points:

- A model of the subpacket structure of a rising-tone lower band chorus element is defined
- Backward-in-time test particle simulation is performed to reconstruct the electron velocity distribution after interaction with chorus
- Perturbed electron distribution features stripes with increased and decreased density which can be partially conserved at short time scales

Corresponding author: M. Hanzelka, mha@ufa.cas.cz

Abstract

We present a test particle study of perturbations of a weakly relativistic electron distribution interacting with a rising-tone lower band chorus emission. Trajectories of interacting electrons are traced back in time from the equator to reconstruct the perturbed velocity distribution. The wave field is precalculated from a model based on the nonlinear growth theory and features a realistic subpacket structure. The perturbed distribution reveals a series of stripes of increased and decreased phase space density. This perturbation is associated with the electromagnetic hole structure which exists along the resonance velocity curve of each subpacket. Time-averaging of the final distribution shows that rising-tone lower band chorus emissions produce a sharp decrease in density at low parallel velocities, which might be detectable by spacecraft particle instruments.

Plain Language Summary

Interaction between plasma waves and particles in the radiation belt has a strong impact on space weather in the Earth's magnetosphere. Here we focus on the interaction of electrons and natural emissions of chorus, which are large-amplitude, right-hand polarized electromagnetic waves with steeply growing wave frequency, abundant in the outer radiation belt. We model the spatial and temporal structure of the waves and obtain a wave packet with realistic behavior of amplitude and frequency. We proceed to simulate the motion of electrons through this wave field and reconstruct the distribution of electrons over velocities after passing through the whole chorus wave packet. Due to the characteristic subpacket structure of chorus emissions, a series of stripes of increased and decreased density appears in the distribution. Some of those features are preserved even after averaging over time and should thus be observable in the inherently time-averaged spacecraft measurements.

1 Introduction

Whistler mode chorus emissions are right-hand circularly polarized electromagnetic waves which occur abundantly in the outer Van Allen radiation belt (Tsurutani & Smith, 1974; Santolík, 2008; Li et al., 2009; Tyler et al., 2019). We distinguish between the lower band chorus, which occupies the frequency range from about 0.1 up to 0.5 of the local electron gyrofrequency Ω_e, and the upper band chorus, which falls into the frequency range

from $0.5\,\Omega_{\mathrm{e}}$ up to about $0.8\,\Omega_{\mathrm{e}}$ (Burtis & Helliwell, 1976). Both types of chorus appear as quasi-monochromatic discrete elements in the time-frequency power spectra with rising or falling frequency (Taubenschuss et al., 2015), typically separated by a gap around $0.5\,\Omega_{\mathrm{e}}$ (Santolík et al., 2003; Gao et al., 2019), with each element consisting of several short wave packets (Santolík et al., 2004). The wave magnetic field in these subpackets can occasionally reach amplitudes up to about $1\,\%$ of the background magnetic field (Santolík et al., 2014). Detailed knowledge of the interaction between electrons and large-amplitude chorus is essential for understanding the dynamics of Earth's magnetosphere (Reeves et al., 2013; Baker et al., 2018).

The chorus emissions are generated by nonlinear interaction between coherent whistler mode waves and resonant electrons in the vicinity of the magnetic equator (LeDocq et al., 1998; Santolík et al., 2004; Omura et al., 2008). The generation process can be studied by the means of full particle simulations (Hikishima et al., 2009), electron hybrid simulations (Katoh & Omura, 2016) or Vlasov hybrid simulations (Nunn et al., 1997), which self-consistently evolve both the wave field and the electron distribution, but are computationally expensive. To predict the growth of wave amplitude and frequency within a single element, the nonlinear growth theory was developed (Omura et al., 2013). This theory was employed by several authors (Summers et al., 2012; Kubota et al., 2018; Omura et al., 2019) to obtain a simple model of the chorus wave field, which can be used for numerical studies of test particle trajectories.
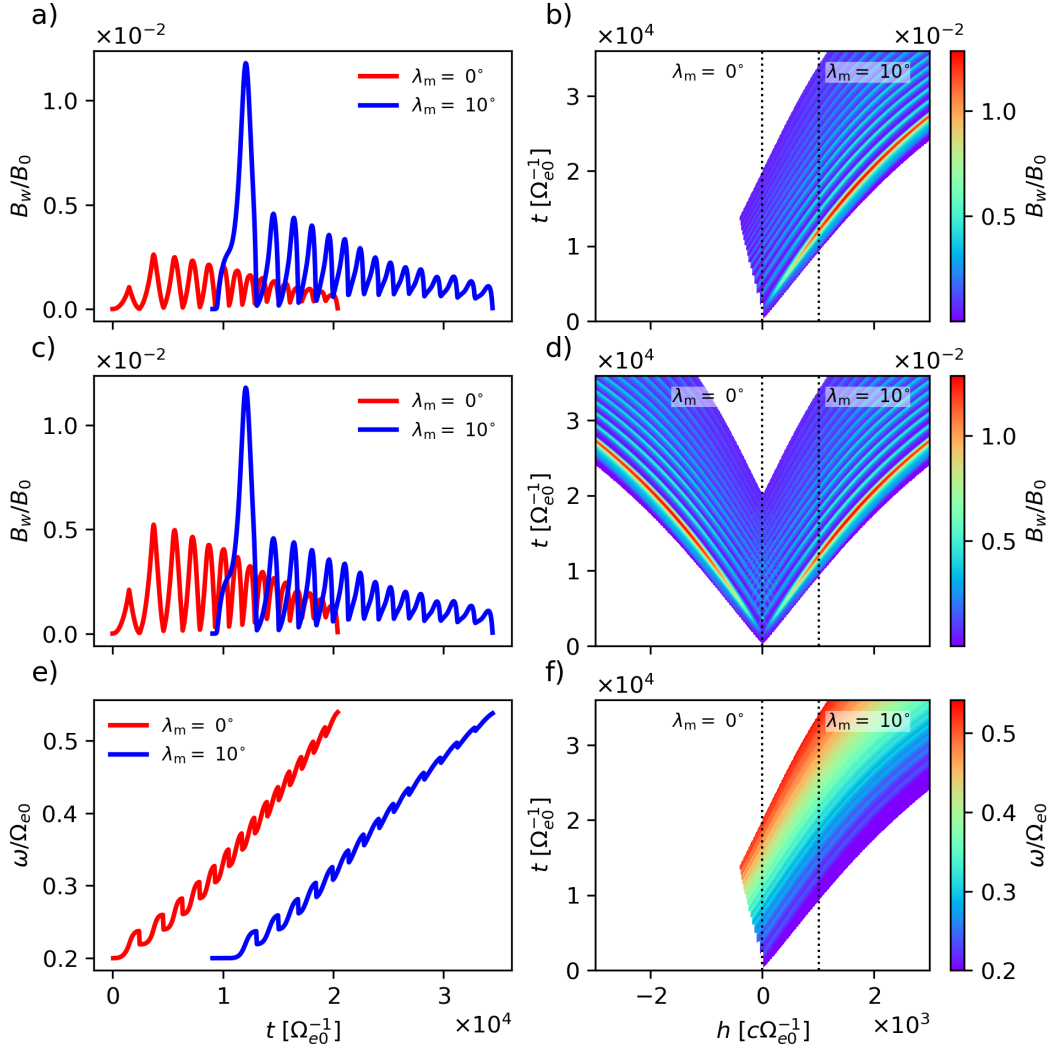
Here we use a model of parallel-propagating lower band chorus to study the perturbations of a weakly relativistic distribution of electrons passing through a single rising-tone chorus element. In Section 2 we explain how the model was improved in the present study to produce slightly more realistic amplitudes and subpacket structure, and the final modeled wave field is briefly described there. To reconstruct the velocity distribution at a chosen point in time and space, we employ the backward-in-time test particle simulation method as described by Nunn and Omura (2015). The concept behind this method and the input parameters chosen in this study are presented in Section 3.1, with its main advantage being the a posteriori choice of the initial velocity distribution. In Section 3.2 we present the computed electron velocity distribution functions. We observe that the interaction with a single subpacket creates stripes of increased and decreased phase space density along the cyclotron resonance velocity curve corresponding to the frequency of the subpacket, which is in accordance with the predicted motion of electrons

in the vicinity of an electromagnetic phase space hole. Depending on the shape of the initial distribution of electrons in parallel and perpendicular velocities, a phase space hill can be observed instead of a hole, After passing through multiple subpackets, the electron velocity distribution is perturbed by several stripes, which are distorted by overlapping and by the adiabatic motion of particles. This is in agreement with results from full particle simulations (Hikishima et al., 2010; Tao et al., 2017). Finally, we show that a time-averaged distribution of particles that passed through the whole chorus element retains some of the features observed, so the presence of these features could be confirmed by analyzing data from spacecraft particle instruments. In Section 4 we summarize our findings and discuss the impact of the perturbations of the distribution on wave generation.

2 Wave model

To obtain the electromagnetic field of a chorus wave propagating along a magnetic field line, we solved a system of differential equations describing the evolution of magnetic wave amplitude B_{w} and frequency ω in the source region and then used transport equations to propagate the wave in space. The method is based on the concept of antenna radiation from the resonant current (Helliwell, 1967; Trakhtengerts et al., 2003) and the chorus equations of the nonlinear growth theory (Omura et al., 2009). The set of solved equations and input parameters can be found in the Supporting Information (SI), Text S1. It is nearly the same model as described by Hanzelka et al. (2020), with the only difference being the suppression of resonant current in downstream regions with overlapping subpackets. The important point here is that the simulated chorus element features a realistic subpacket structure with irregular growth in frequency and an upstream shift of the source region – these properties have been observed in numerical simulations and spacecraft measurements (Hikishima et al., 2009; Santolík et al., 2014; Foster et al., 2017).

The magnetic field amplitudes of the model chorus element are shown in Figures 1a and 1b. As a further improvement to the wave model, we consider waves propagating in both directions, as shown in the amplitude plots in Figures 1c and 1d. The electric and magnetic fields are summed in the equatorial region, with phases being set to zero at the beginning of each subpacket. This results in doubling the amplitude B_{w} at points of matching phases, notably in the source of the first subpacket. However, for the

Figure 1. The chorus wave field used in our test particle simulations. a) Time evolution of wave magnetic field amplitude B_w at latitudes $\lambda_m = 0°$ (red line) and $\lambda_m = 10°$ (blue line). b) Evolution of B_w in time and space with dotted lines showing the spatial cuts at $\lambda_m = 0°$ and $\lambda_m = 10°$. c) and d) are same as a) and b), but for the total wave field obtained as a superposition of left- and right-propagating waves. e) and f) show the wave frequency ω and copy the format of panels a) and b). The time duration of the chorus element at the equator is $340\,\text{ms}$.

cyclotron resonance, only the wave which propagates against the motion of the traced electron is important. Finally, Figures 1e and 1f show the growth of frequency within the subpackets, ranging from $0.20\,\Omega_{e0}$ to $0.53\,\Omega_{e0}$, where Ω_{e0} is the equatorial gyrofrequency. The simulation was stopped when the starting frequency of the next subpacket

would become higher than $0.5\,\Omega_{\mathrm{e0}}$; the upper frequency limit is arbitrary as there is no natural cutoff for strictly parallel lower band chorus.

3 Particle Simulation

3.1 Methods and Initial Conditions

The simulation method used in this research letter is based on the test particle simulation approach presented by Nunn and Omura (2015). It utilizes Liouville's theorem which states that in a Hamiltonian system, the phase space density along particle trajectories remains constant. Therefore, we can take a sample of particles that uniformly covers a certain region of the phase space and reconstruct the velocity distribution function at a certain point (t, h) by tracking the particles back in time to another point where the phase space density is known. This allows us to choose the initial velocity distribution after conducting the simulation without any considerable computational cost. Also, we can sample arbitrarily small regions of the phase space, allowing us to achieve high local resolution even with a low number of particles.

Since the phase space density is supposed to be preserved in our physical system, the initial velocity distribution function must evolve adiabatically along field lines. We choose a distribution in the form (Summers et al., 2012)

$$f(u_\parallel, u_\perp, h)\mathrm{d}^3 u = \frac{N_{\mathrm{he,eq}}}{(2\pi)^{\frac{3}{2}} U_{\parallel\mathrm{eq}} U_{\perp\mathrm{eq}}^2} \exp\left(-\frac{u_\parallel^2}{2U_{\parallel\mathrm{eq}}^2} - \frac{u_\perp^2}{2U_{\perp\mathrm{eq}}^2}\left(\left(1 - \frac{B_{\mathrm{eq}}}{B(h)}\right)\frac{U_{\perp\mathrm{eq}}^2}{U_{\parallel\mathrm{eq}}^2} + \frac{B_{\mathrm{eq}}}{B(h)}\right)\right)\mathrm{d}^3 u\,, \tag{1}$$

$$\mathrm{d}^3 u = \mathrm{d}u_\parallel u_\perp \mathrm{d}u_\perp \mathrm{d}\varphi\,, \tag{2}$$

which is a bi-Maxwellian distribution in relativistic velocities $u_\parallel$, $u_\perp$, and also the first order expansion of the Maxwell-Jüttner distribution in velocity and temperature. In velocities $v_\parallel = u_\parallel/\gamma$, $v_\perp = u_\perp/\gamma$, the distribution takes form

$$f(v_\parallel, v_\perp, h)\mathrm{d}^3 v = \frac{N_{\mathrm{he,eq}}}{(2\pi)^{\frac{3}{2}} V_{\parallel\mathrm{eq}} V_{\perp\mathrm{eq}}^2} \exp\left(-\frac{v_\parallel^2}{2V_{\parallel,\mathrm{eq}}^2} - \frac{v_\perp^2}{2V_{\perp\mathrm{eq}}^2}\left(\left(1 - \frac{B_{\mathrm{eq}}}{B(h)}\right)\frac{V_{\perp\mathrm{eq}}^2}{V_{\parallel\mathrm{eq}}^2} + \frac{B_{\mathrm{eq}}}{B(h)}\right)\right)\gamma^4(1 - \frac{v_\parallel^2}{c^2})(1 - \frac{v_\perp^2}{c^2})\mathrm{d}^3 v\,, \tag{3}$$

$$\mathrm{d}^3 v = \mathrm{d}v_\parallel v_\perp \mathrm{d}v_\perp \mathrm{d}\varphi\,. \tag{4}$$

Distribution along the particle phases φ is set to be uniform. $N_{\mathrm{he,eq}}$ stands here for the hot electron density at the equator, $V_{\parallel\mathrm{eq}}$ ($U_{\parallel\mathrm{eq}}$) and $V_{\perp\mathrm{eq}}$ ($U_{\perp\mathrm{eq}}$) are the equatorial thermal (relativistic) velocities and $B(h)$ is the magnetic dipole field strength along the field line.

140   To integrate the motion of electrons we use the phase-volume preserving Boris method

141   as described by Higuera and Cary (2017) without the standard phase approximation (see

142   e.g. Zenitani and Umeda (2018) for a discussion on Boris solvers). Particles are traced

143   until they leave the wave field, with the inclusion of the possibility of encountering the

144   wave after reflection at the mirror point. Time steps are fixed and chosen in such way

145   that there are always at least 50 steps per gyroperiod along all trajectories. Although

146   this is a rather low number, the numerical errors in phase space density in the regions

147   of the velocity distribution we are interested in are orders of magnitude smaller than the

148   typical magnitude of perturbations introduced by the resonant interaction.

149   The choice of input parameters common to all simulation runs is the following: $\omega_{\mathrm{phe}} =$

150    $0.3\,\Omega_{\mathrm{e}0}$, where $N_{\mathrm{he,eq}} = \omega_{\mathrm{phe}}^2 m\varepsilon_0/e^2$, $U_{\|\mathrm{eq}} = 0.12\,c$, $U_{\perp\mathrm{eq}} = 0.25\,c$. The background

151   magnetic field is assumed to be dipolar with equatorial strength at the Earth's surface

152    $3.1 \cdot 10^{-5}\,\mathrm{T}$ and the particles are propagating on the L-shell $L = 4.5$. The correspond-

153   ing equatorial electron gyrofrequency evaluates to $\Omega_{\mathrm{e}0} = 5.98 \cdot 10^4\,\mathrm{s}^{-1}$. These parame-

154   ters are the same as in the wave simulation (see the SI, Text S1). To reduce the size of

155   the wave field array, the information about wave amplitude, wave frequency and wave

156   magnetic field phase is saved in spatial bins $\Delta h = 8\,c\Omega_{\mathrm{e}0}^{-1}$ and time bins $\Delta t = 60\,\Omega_{\mathrm{e}0}^{-1}$

157   and bilinearly interpolated along particle trajectories. To prove that such filtering is ac-

158   ceptable, we calculated the distribution function in Figure 2 also with a wave field given

159   on a finer grid, $\Delta h = 1\,c\Omega_{\mathrm{e}0}^{-1}$, $\Delta t = 4\,\Omega_{\mathrm{e}0}^{-1}$. We observed no qualitative changes be-

160   tween the two perturbed distributions. Quantitative assessment is difficult as even a tiny

161   change in the wave field can cause a particle to evade trapping, thus completely chang-

162   ing the phase space density of the bin the particle represents. As a simple measure of

163   the changes we chose to compare the absolute maxima of the density change due to par-

164   ticle interaction. In both cases they appear at the same parallel velocity and differ in mag-

165   nitude by less than 2 %.

3.2 Results

167   The first simulation was started at the equator at time $t_{\mathrm{ini}} = 2520\,\Omega_{\mathrm{e}0}^{-1}$, which cor-

168   responds to the point where the first subpacket ends. Initial velocities and phases were

169   sampled uniformly, $v_{\|} \in (-0.5\,c, 0.0\,c)$ with 256 points, $v_{\perp} \in (0.0\,c, 1.0\,c)$ with 256 points,

170    $\varphi \in [0, 2\pi)$ with 128 points (particles with initial velocities larger than c are excluded

171   from the sample). The obtained perturbed distribution was integrated over φ and is shown

172   in Figure 2a, normalized to $f_{0\max} = \max_{(v_\parallel, v_\perp)} f_0(v_\parallel, v_\perp)$. In Figure 2b the reduced

173   distribution $f(v_\parallel)$ is presented and compared to the initial (unperturbed) distribution

174    $f_0(v_\parallel)$, showing a plateau around $v_\parallel = -0.19\,c$. The difference $f(v_\parallel, v_\perp) - f_0(v_\parallel, v_\perp)$

175   is shown in Figure 2c and reveals that a stripe has formed in the perturbed phase space

176   density distribution. A region of increased density is situated along the relativistic res-

177   onance velocity curve corresponding to the initial frequency of the subpacket, and a re-

178   gion of decreased density lies along the resonance velocity curve corresponding to the fi-

179   nal frequency of the subpacket. This structure is the remnant of an electromagnetic phase

180   space hole. The time evolution of the hole in time can be seen in the SI, Movie S1. It

181   should be mentioned here that the relativistic cyclotron resonance velocity V_R forms an

182   elliptical arc in the $(v_\parallel, v_\perp)$ space (Wu, 1985).

183   In Figure 2d we show again the difference $f(v_\parallel, v_\perp) - f_0(v_\parallel, v_\perp)$, but for an ini-

184   tial distribution with $U_{\parallel\mathrm{eq}} = 0.25\,c = U_{\perp\mathrm{eq}}$, that is, for an isotropic distribution (equa-

185   torial thermal anisotropy $A_{\mathrm{eq}} = U_{\perp\mathrm{eq}}^2 / U_{\parallel\mathrm{eq}}^2 - 1 = 0.0$). Such a distribution is not con-

186   sistent with the underlying wave model, but helps us to better understand the transport

187   of phase space density. The perturbation is now less prominent, but more importantly,

188   the regions of increased and decreased density within the stripe are switched. So, in this

189   case, the stripe is the remnant of an electromagnetic phase space hill. The explanation

190   for this behavior is sketched in Figure 2e. Untrapped particles that are scattered by the

191   whistler wave decrease their kinetic energies and pitch angles, while the particles which

192   are transported along the trapping region increase their kinetic energies and pitch an-

193   gles (see e.g. Vainchtein et al. (2018) and reference therein, and the Movies S2 and S3

194   in the SI). Depending on the shape of contours of the phase space distribution, a phase

195   space hole or a phase space hill will be produced. While the hole is associated with rising-

196   tone emissions, the hill is associated with fallers (Nunn & Omura, 2012) and would de-

197   plete the free energy stored in risers. Therefore, to tell whether a rising-tone chorus can

198   grow in the equatorial region, we need to know the full 2D velocity distribution, or at

199   the very least the phase space density in $>V_{\mathrm{tr}}$ range around the resonance velocity curve.

200   The second simulation was started at the equator at time $t_{\mathrm{ini}} = 21000\,\Omega_{\mathrm{e}0}^{-1}$, which

201   is immediately after the end of the last subpacket. The perturbed velocity distribution

202   is shown in Figure 3a. The reduced distribution is now presented as a difference $f(v_\parallel) -$

203    $f_0(v_\parallel)$, showing a very prominent decrease in phase space density around $v_\parallel = -0.06\,c$,

204   which corresponds to the resonance velocity of the last subpacket. In Figure 3c we can

see that the stripes in $f(v_\parallel, v_\perp) - f_0(v_\parallel, v_\perp)$ plot are still present, but their structure is getting less clear with decreasing parallel velocity. The stripes are also bent out towards higher $|v_\parallel|$, which is the result of the adiabatic motion of particles that interacted with lower frequency subpackets further away from the equator. The time evolution of the velocity distribution is shown in the SI, Movie S4. We also show pitch-angle distributions $f(\alpha)$ for logarithmically spaced energy bins in Figure 3d, as it is the common data product of measurements done by spacecraft particle instruments. A feature not seen in the previous simulation is the wide transverse stripe at high energies and pitch angles (Figure 3c) – it is caused by particles that interacted with both the left- and right-propagating wave at different places. This would not happen in elements with a shorter time duration. See Figures S1 and S2 in the SI for an example trajectory of such particles. Figures 3e and 3f present perturbed distributions for initial velocity distribution with anisotropy $A_{\mathrm{eq}} = 0.36$. The results show that even when a certain distribution supports formation of electron hole at larger resonance velocities, it might change at lower velocities, even for a simple near-Maxwellian model.

All the plots in Figure 3 show the distribution function at a single point in time. To obtain results that are comparable with spacecraft particle measurements, we need to average the data over time. We chose six time points from $t = 21000\,\Omega_{\mathrm{e0}}^{-1}$ to $t = 28500\,\Omega_{\mathrm{e0}}^{-1}$ with a step of $1500\,\Omega_{\mathrm{e0}}^{-1}$, which translates approximately to a $125\,\mathrm{ms}$ time span. For comparison, the PEACE (Plasma Electron And Current Experiment) instrument on Cluster spacecraft can measure a partial distribution in a $15°$ polar angle bin within about 60 milliseconds (Johnstone et al., 1997). The Magnetospheric MultiScale (MMS) mission measures the full three-dimensional (3D) electron distribution in $30\,\mathrm{ms}$ with a polar angle resolution of 9-15° (Pollock et al., 2016).

The 3D velocity distributions obtained from simulations were first averaged and then used for further calculations. Figure 4a shows the averaged velocity distribution in $(v_\parallel, v_\perp)$ space, revealing that the stripe structure has been mostly lost. The difference between perturbed and initial reduced distributions $f(v_\parallel) - f_0(v_\parallel)$ in Figure 4b shows that the prominent depletion at low $|v_\parallel|$ is still present. This is visible as well in Figure 4c, which also depicts the decrease of phase space density at high energies and pitch angles in favor of the low-energy low-pitch-angle region. Figure 4d further confirms this behavior by showing the pitch angle distribution in separate energy bins. Based on these results of time-averaging, we do not expect the stripe structure to be visible in particle mea-

surements, but the depletion at resonance velocity corresponding to the highest frequency of the chorus element should be measurable.

4 Discussion and Conclusions

We have investigated the interaction of resonant electrons with a lower band chorus element by the means of test particle simulations. Because this type of simulation does not produce any self-consistent electromagnetic wave field, the credibility of the results is dependent on the quality of the underlying model of chorus emissions. In construction of the wave field model, we attempted to include several properties that were observed in numerical simulations and spacecraft measurements or theoretically predicted: presence of a subpacket structure (Santolík et al., 2004), drift of the source region (Hikishima et al., 2009; Demekhov et al., 2020), localized decreases in frequency between adjacent subpackets (Santolík et al., 2014) and suppression of convective growth due to overlap of adjacent subpackets. Despite these improvements, the only way to determine whether the model truly is sufficiently consistent is to calculate the evolution of resonant current from the perturbed velocity distributions and see if it matches with the regions of amplitude and frequency growth. We plan to investigate this in future studies. The results of simulation of interaction with one subpacket assure us that the highly anisotropic initial velocity distribution of hot electrons we assumed is consistent with creation of an electromagnetic phase space hole that can provide the current for amplitude growth. On the other hand, we have shown that an isotropic, almost Maxwellian distribution would not support a rising-tone chorus emission, because the transport of particles in $(v_\parallel, v_\perp)$ space would then require extraction of energy from the wave.

In the second simulation, where we focused on the interaction with an entire chorus element, we chose an element with a rather long time duration of almost $350\,\text{ms}$ (compare with e.g. Teng et al. (2017)). Because there is no natural upper frequency cutoff in the model, we artificially cut the wave spectrum at around $0.5\,\Omega_{\text{e0}}$. Cutting the element off at the more typically observed frequencies of about $0.40\,\Omega_{\text{e0}}$ to $0.45\,\Omega_{\text{e0}}$ (Santolik et al., 2008; Gao et al., 2019) would shorten the time duration by 60 to 100 milliseconds. However, having longer elements allows for electron interaction with the wave propagating to negative h values, resulting in the transverse stripe in densities observed in Figures 3c and 4c (see also SI, Figure S1). These electrons slightly disturb the stripe struc-

ture in the perturbed distribution and should not be neglected in general, although the effect is rather small.

The stripe structure that appears in the perturbed distribution function is the most interesting result of this study. Specific appearance of this structure is influenced by multiple factors: wave amplitude, wave frequency (or resonance velocity), number of subpackets (or more specifically, their frequency spacing) and the initial velocity distribution are the most important. As the frequency spacing between subpackets decreases and the resonance velocity moves to lower absolute values, the stripes will have an increasing amount of overlap. This means that at one point, the waves will start entrapping significant amounts of particles from the high-density part of the previous stripe (see the second half of Movie S1 where this effect appears due to large overlap of frequency ranges of the adjacent subpackets). This decreases the effectivity of energy exchange between the particles and the wave and results in the distorted stripe structure which we can see around $v_\parallel = -0.1\,c$ in Figure 3c. In a self-consistent simulation, this would lead to a decrease in wave amplitude – this is partly included in our model through the suppression of resonant current (Equations 14 and 15 in the SI), which leads to a weaker convective growth of wave amplitudes. A natural suppression of resonant current is described in the self-consistent particle simulation results of Hikishima et al. (2010) and Tao et al. (2017). However, in their case the suppression comes also from the shape of the velocity distribution they use, which excludes particles at low perpendicular velocities. As a result, the electromagnetic phase space hole at high pitch angles changes to a hill and averages out the total resonant current to zero. We can see a similar effect in Figure 3e for the low-anisotropy distribution, where the trapped particles at high frequencies have higher density then the untrapped scattered particles.

From the experimental point of view, the most interesting feature of the perturbed distribution is the density decrease along resonance velocity curve of the highest frequency element. This density depletion persists even after time averaging. However, the linear growth theory suggest that the density depression will quickly form a plateau due to strong anisotropic instability (see pitch-angle anisotropies in the SI, Movie S5). Results of future work will show if this predicted density structure might be confirmed experimentally using data from particle detectors. Figure 4c shows that although a rather coarse binning in energy is sufficient (units to tens of keV), a pitch-angle resolution better than 15° will be required to properly discern the observed structure. In particle-in-cell sim-

ulations (Hikishima et al., 2010; Tao et al., 2017), the density depletion was observed as well, which gives further credence to our use of test particle simulations on the background of a realistic wave model, as it proves that the linear growth is not so significant. The reason for the persistence of the position of this perturbation in phase space is 1) negligible effect of adiabatic motion near the equator and 2) small changes in resonance velocity between the higher frequency subpackets. The density depletion could become less prominent if the amplitudes decreased very gradually with frequency down to zero. However, the spectral gap seems to produce rather sharp drop-offs in the spectral power (see e.g. Santolík et al. (2004)).

To conclude, we have shown that test particle simulations reveal a stripe structure in a velocity distribution of electrons interacting with a rising-tone lower band chorus emission. Part of the stripe structure persists even in time averaged data, promising the possibility of detecting it with spacecraft particle measurements. All the results we presented here can be easily recalculated for any possible initial distribution, and can also be used for the calculation of resonant currents, providing thus a possibility for further in-depth studies of chorus wave growth.

References

Baker, D. N., Erickson, P. J., Fennell, J. F., Foster, J. C., Jaynes, A. N., & Verronen, P. T. (2018, February). Space Weather Effects in the Earth's Radiation Belts. *Space Science Reviews*, *214*(1), 17. doi: 10.1007/s11214-017-0452-7

Burtis, W. J., & Helliwell, R. A. (1976, November). Magnetospheric chorus: Occurrence patterns and normalized frequency. *Planetary and Space Science*, *24*(11), 1007-1010,IN1-IN4,1011-1024. doi: 10.1016/0032-0633(76)90119-7

Demekhov, A. G., Taubenschuss, U., Hanzelka, M., & Santolík, O. (2020, March). Frequency Dependence of Very Low Frequency Chorus Poynting Flux in the

Source Region: THEMIS Observations and a Model. *Geophysical Research Letters*, *47*(6), e86958. doi: 10.1029/2019GL086958

Foster, J. C., Erickson, P. J., Omura, Y., Baker, D. N., Kletzing, C. A., & Claude-pierre, S. G.   (2017, Jan).   Van Allen Probes observations of prompt MeV radiation belt electron acceleration in nonlinear interactions with VLF chorus.   *Journal of Geophysical Research (Space Physics)*, *122*(1), 324-339.   doi: 10.1002/2016JA023429

Gao, X., Chen, L., Li, W., Lu, Q., & Wang, S.   (2019, April).   Statistical Results of the Power Gap Between Lower-Band and Upper-Band Chorus Waves.   *Geophysical Research Letters*, *46*(8), 4098-4105. doi: 10.1029/2019GL082140

Hanzelka, M., Santolík, O., Omura, Y., Kolmašová, I., & Kletzing, C. A.   (2020).   A model of the subpacket structure of rising tone chorus emissions.
doi: 10.1002/essoar.10503189.1

Helliwell, R. A.   (1967, Oct).   A theory of discrete VLF emissions from the magnetosphere.   *Journal of Geophysical Research*, *72*(19), 4773-4790.   doi: 10.1029/JZ072i019p04773

Higuera, A. V., & Cary, J. R.   (2017, May).   Structure-preserving second-order integration of relativistic charged particle trajectories in electromagnetic fields.   *Plasma Physics*, *24*(5), 052104. doi: 10.1063/1.4979989

Hikishima, M., Omura, Y., & Summers, D. (2010, Dec). Self-consistent particle simulation of whistler mode triggered emissions.   *Journal of Geophysical Research (Space Physics)*, *115*(A12), A12246. doi: 10.1029/2010JA015860

Hikishima, M., Yagitani, S., Omura, Y., & Nagano, I.   (2009, January).   Full particle simulation of whistler-mode rising chorus emissions in the magnetosphere.   *Journal of Geophysical Research (Space Physics)*, *114*, A01203.   doi: 10.1029/2008JA013625

Johnstone, A. D., Alsop, C., Burge, S., Carter, P. J., Coates, A. J., Coker, A. J., ... Woodliffe, R. D. (1997, January). Peace: a Plasma Electron and Current Experiment. *Space Science Reviews*, *79*, 351-398. doi: 10.1023/A:1004938001388

Katoh, Y., & Omura, Y.   (2016, November).   Electron hybrid code simulation of whistler-mode chorus generation with real parameters in the Earth's inner magnetosphere.   *Earth, Planets and Space*, *68*, 192.   doi: 10.1186/s40623-016-0568-0
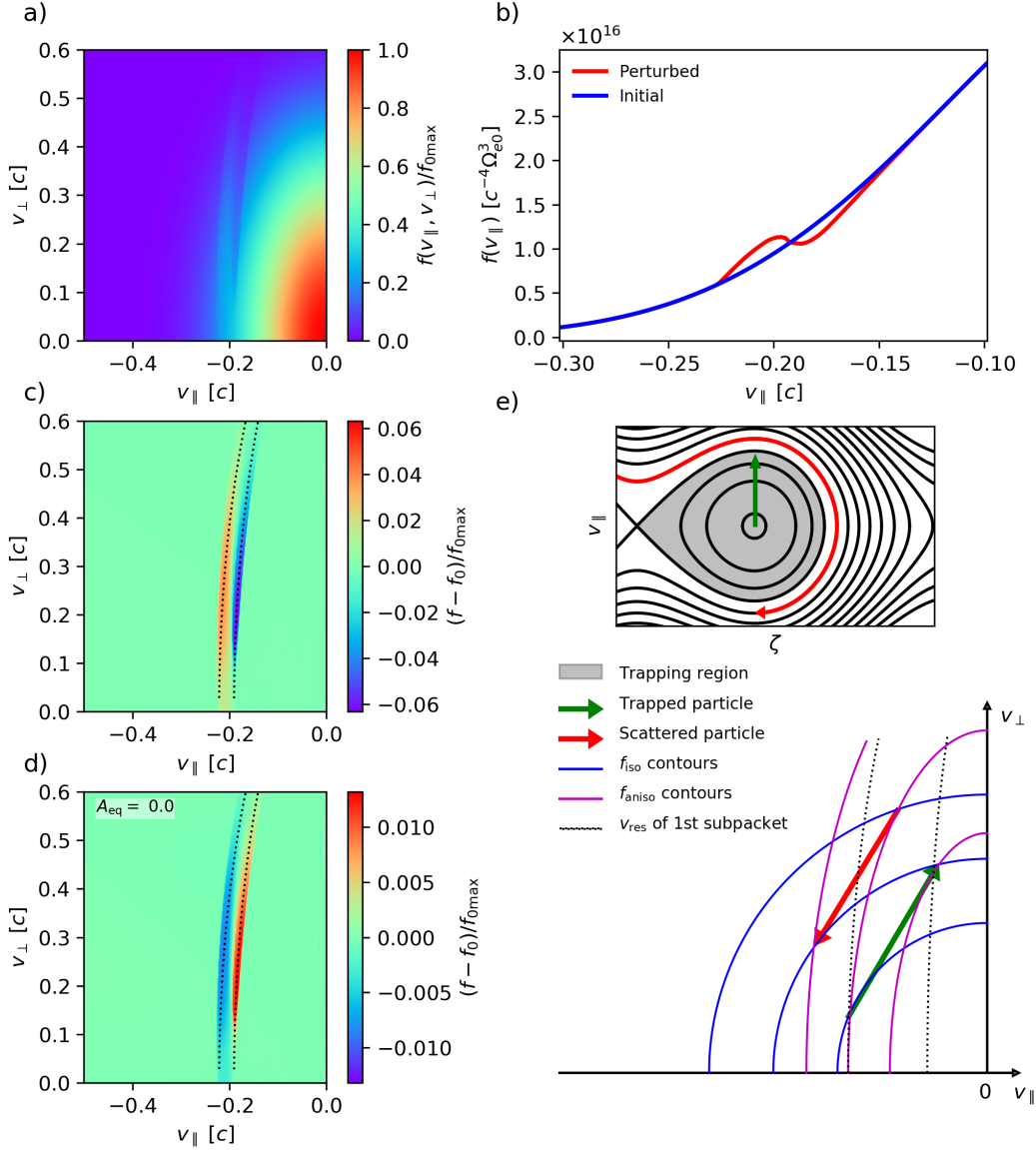
Kubota, Y., Omura, Y., Kletzing, C., & Reeves, G. (2018, April). Generation process of large-amplitude upper band chorus emissions observed by Van Allen Probes. *Journal of Geophysical Research (Space Physics)*, *123*, 3704-3713. doi: 10.1029/2017JA024782

LeDocq, M. J., Gurnett, D. A., & Hospodarsky, G. B. (1998, January). Chorus source locations from VLF Poynting flux measurements with the Polar spacecraft. *Geophysical Research Letters*, *25*, 4063-4066. doi: 10.1029/1998GL900071

Li, W., Thorne, R. M., Angelopoulos, V., Bortnik, J., Cully, C. M., Ni, B., ... Magnes, W. (2009, May). Global distribution of whistler-mode chorus waves observed on the THEMIS spacecraft. *Geophysical Research Letters*, *36*(9), L09104. doi: 10.1029/2009GL037595

Nunn, D., & Omura, Y. (2012, August). A computational and theoretical analysis of falling frequency VLF emissions. *Journal of Geophysical Research (Space Physics)*, *117*(A8), A08228. doi: 10.1029/2012JA017557

Nunn, D., & Omura, Y. (2015, Apr). A computational and theoretical investigation of nonlinear wave-particle interactions in oblique whistlers. *Journal of Geophysical Research (Space Physics)*, *120*(4), 2890-2911. doi: 10.1002/2014JA020898

Nunn, D., Omura, Y., Matsumoto, H., Nagano, I., & Yagitani, S. (1997, December). The numerical simulation of VLF chorus and discrete emissions observed on the Geotail satellite using a Vlasov code. *Journal of Geophysical Research*, *102*(A12), 27083-27098. doi: 10.1029/97JA02518

Omura, Y., Hikishima, M., Katoh, Y., Summers, D., & Yagitani, S. (2009, Jul). Nonlinear mechanisms of lower-band and upper-band VLF chorus emissions in the magnetosphere. *Journal of Geophysical Research (Space Physics)*, *114*(A7), A07217. doi: 10.1029/2009JA014206

Omura, Y., Hsieh, Y.-K., Foster, J. C., Erickson, P. J., Kletzing, C. A., & Baker, D. N. (2019, Apr). Cyclotron Acceleration of Relativistic Electrons Through Landau Resonance With Obliquely Propagating Whistler-Mode Chorus Emissions. *Journal of Geophysical Research (Space Physics)*, *124*(4), 2795-2810. doi: 10.1029/2018JA026374

Omura, Y., Katoh, Y., & Summers, D. (2008, April). Theory and simulation of the generation of whistler-mode chorus. *Journal of Geophysical Research (Space Physics)*, *113*, A04223. doi: 10.1029/2007JA012622

Omura, Y., Nunn, D., & Summers, D. (2013). Generation Processes of Whistler Mode Chorus Emissions: Current Status of Nonlinear Wave Growth Theory. In *Dynamics of the earth's radiation belts and inner magnetosphere* (p. 243-254). American Geophysical Union (AGU). doi: 10.1029/2012GM001347

Pollock, C., Moore, T., Jacques, A., Burch, J., Gliese, U., Saito, Y., ... Zeuch, M. (2016, March). Fast Plasma Investigation for Magnetospheric Multiscale. *Space Science Reviews*, *199*(1-4), 331-406. doi: 10.1007/s11214-016-0245-4

Reeves, G. D., Spence, H. E., Henderson, M. G., Morley, S. K., Friedel, R. H. W., Funsten, H. O., ... Niehof, J. T. (2013, August). Electron Acceleration in the Heart of the Van Allen Radiation Belts. *Science*, *341*(6149), 991-994. doi: 10.1126/science.1237743

Santolík, O. (2008, July). New results of investigations of whistler-mode chorus emissions. *Nonlinear Processes in Geophysics*, *15*(4), 621-630. doi: 10.5194/npg-15-621-2008

Santolík, O., Gurnett, D., & Pickett, J. (2004, July). Multipoint investigation of the source region of storm-time chorus. *Annales Geophysicae*, *22*, 2555-2563. doi: 10.5194/angeo-22-2555-2004

Santolík, O., Gurnett, D. A., Pickett, J. S., Parrot, M., & Cornilleau-Wehrlin, N. (2004, Jan). A microscopic and nanoscopic view of storm-time chorus on 31 March 2001. *Geophysical Research Letters*, *31*(2), L02801. doi: 10.1029/2003GL018757

Santolík, O., Kletzing, C. A., Kurth, W. S., Hospodarsky, G. B., & Bounds, S. R. (2014, January). Fine structure of large-amplitude chorus wave packets. *Geophysical Research Letters*, *41*, 293-299. doi: 10.1002/2013GL058889

Santolik, O., Macusova, E., Titova, E. E., Kozelov, B. V., Gurnett, D. A., Pickett, J. S., ... Demekhov, A. G. (2008, June). Frequencies of wave packets of whistler-mode chorus inside its source region: a case study. *Annales Geophysicae*, *26*(6), 1665-1670. doi: 10.5194/angeo-26-1665-2008

Santolík, O., Parrot, M., & Lefeuvre, F. (2003, February). Singular value decomposition methods for wave propagation analysis. *Radio Science*, *38*, 10-1. doi: 10
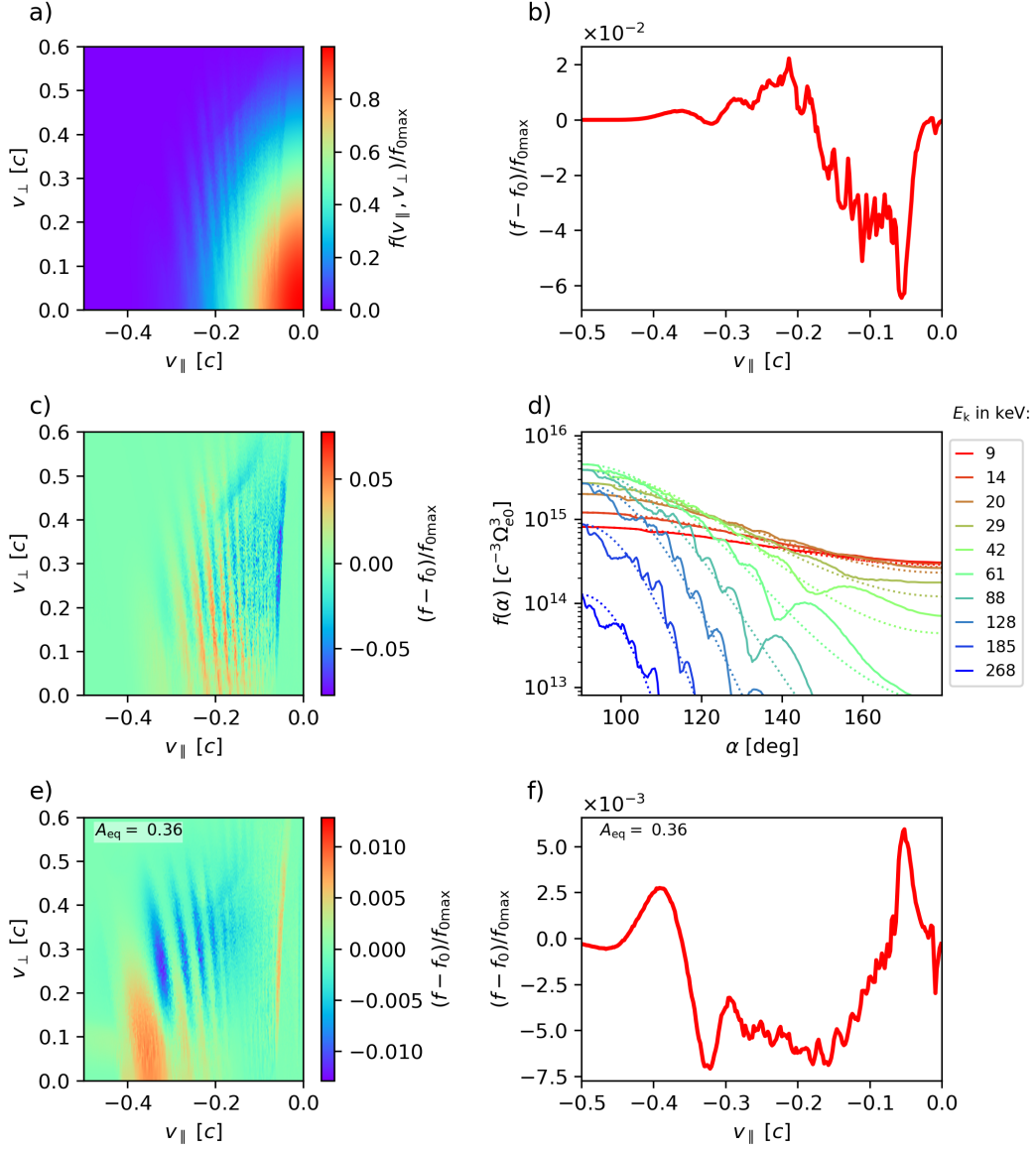
.1029/2000RS002523

Summers, D., Omura, Y., Miyashita, Y., & Lee, D.-H.   (2012, Sep).   Nonlinear spatiotemporal evolution of whistler mode chorus waves in Earth's inner magnetosphere.   *Journal of Geophysical Research (Space Physics)*, *117*(A9), A09206. doi: 10.1029/2012JA017842

Tao, X., Zonca, F., & Chen, L.   (2017, April).   Identify the nonlinear wave-particle interaction regime in rising tone chorus generation.   *Geophysical Research Letters*, *44*(8), 3441-3446. doi: 10.1002/2017GL072624

Taubenschuss, U., Santolík, O., Graham, D. B., Fu, H., Khotyaintsev, Y. V., & Le Contel, O.   (2015, October).   Different types of whistler mode chorus in the equatorial source region. *Geophysical Research Letters*, *42*(20), 8271-8279. doi: 10.1002/2015GL066004

Teng, S., Tao, X., Xie, Y., Zonca, F., Chen, L., Fang, W. B., & Wang, S.   (2017, December).   Analysis of the Duration of Rising Tone Chorus Elements. *Geophysical Research Letters*, *44*(24), 12,074-12,082. doi: 10.1002/2017GL075824

Trakhtengerts, V. Y., Demekhov, A. G., Hobara, Y., & Hayakawa, M.   (2003). Phase-bunching effects in triggered vlf emissions: Antenna effect.   *Journal of Geophysical Research (Space Physics)*, *108*(A4). doi: 10.1029/2002JA009415

Tsurutani, B. T., & Smith, E. J.   (1974, Jan).   Postmidnight chorus: A substorm phenomenon. *Journal of Geophysical Research*, *79*(1), 118-127.   doi: 10.1029/ JA079i001p00118

Tyler, E., Breneman, A., Cattell, C., Wygant, J., Thaller, S., & Malaspina, D. (2019, March).   Statistical Occurrence and Distribution of High-Amplitude Whistler Mode Waves in the Outer Radiation Belt.   *Geophysical Research Letters*, *46*(5), 2328-2336. doi: 10.1029/2019GL082292

Vainchtein, D., Zhang, X. J., Artemyev, A. V., Mourenas, D., Angelopoulos, V., & Thorne, R. M.   (2018, October).   Evolution of Electron Distribution Driven by Nonlinear Resonances With Intense Field-Aligned Chorus Waves. *Journal of Geophysical Research (Space Physics)*, *123*(10), 8149-8169.   doi: 10.1029/2018JA025654

Wu, C. S.   (1985, August).   Kinetic cyclotron and synchrotron maser instabilities: Radio emission processes by direct amplification of radiation.   *Space Science Reviews*, *41*(3-4), 215-298. doi: 10.1007/BF00190653
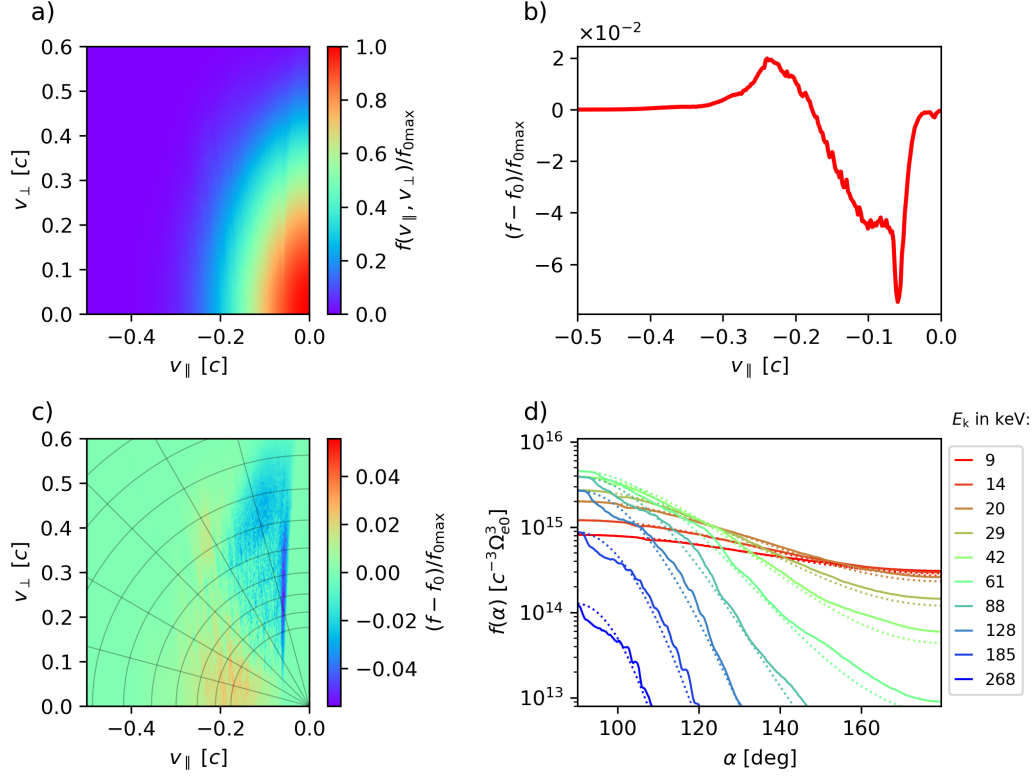
464 Zenitani, S., & Umeda, T. (2018, November). On the Boris solver in particle-in-cell

465   simulation. *Plasma Physics*, *25*(11), 112110. doi: 10.1063/1.5051077

Figure 2. a-d) Perturbation of electron velocity distribution after interaction with one chorus subpacket, simulation starting at point $t = 2520\,\Omega_{e0}^{-1}$, $h = 0\,c\Omega_{e0}^{-1}$. a) 2D velocity distribution normalized to the maximum phase space density f_{0max} at $v_\parallel = 0$, $v_\perp = 0$. b) Velocity distribution integrated over perpendicular velocities, comparison of perturbed distribution (blue line) with initial distribution (red line). c) Difference between perturbed and initial velocity distribution in $(v_\parallel, v_\perp)$ space, normalized to f_{0max}. d) Same as c), but for initial distribution with zero temperature anisotropy. e) Schematic explanation of the motion of resonant particles. The first illustration shows the electromagnetic phase space hole in $(\zeta, v_\parallel)$ space, where ζ is the angle between the wave magnetic field vector and the perpendicular velocity of electrons. Green arrow represents the direction of motion of the trapping region (in grey) to lower $|v_\parallel|$, red arrow shows the motion of untrapped resonant particles. The streamlines in the phase space are only illustrative and do not represent the full dynamics. In the second diagram, the the types of motion are illustrated in the $(v_\parallel, v_\perp)$ space. Blue and purple lines show the contours of phase space density of an isotropic and a highly anisotropic distribution, respectively. Dotted black lines indicate the resonance velocity curves for the lowest and highest frequency within the subpacket.

Figure 3. Perturbation of electron velocity distribution after interaction with a whole chorus element, simulation starting at point $t = 21000\,\Omega_{e0}^{-1}$, $h = 0\,c\Omega_{e0}^{-1}$. a), b) and c) have the same format as in Figure 2, but now the panel b) shows the difference between perturbed and initial reduced distribution, instead of their comparison. d) Pitch angle distribution in logarithmically spaced energy bins. The listed values of E_k represent the geometric mean of each bin. e) Same as c), but for a distribution with equatorial thermal anisotropy $A_{eq} = 0.36$. f) is the same as b), but for $A_{eq} = 0.36$.

Figure 4. Same plots as in Figure 3a-d, but for velocity distributions time-averaged on the interval from $21000\,\Omega_{e0}^{-1}$ to $t = 28500\,\Omega_{e0}^{-1}$, i. e. an interval of about 125 milliseconds starting at the end of the last subpacket. In panel c), pitch angle bins of $15°$ and energy bins according to panel d) are plotted with grey lines.